

Article

Sedimentary Setting and Ore-Forming Model in the Songtao Manganese Deposit, Southwestern China: Evidence from Audio-Frequency Magnetotelluric and Gravity Data

Lingfeng Gao ¹, Shan Xu ^{1,*}, Xiangyun Hu ^{1,2} , Shuang Liu ¹ , Qi Zhou ³ and Bingnan Yang ⁴

¹ Institute of Geophysics and Geomatics, China University of Geosciences, Wuhan 430074, China; gaolf@cug.edu.cn (L.G.); xyhu@cug.edu.cn (X.H.); lius@cug.edu.cn (S.L.)

² State Key Laboratory of Geological Processes and Mineral Resources, China University of Geosciences, Wuhan 430074, China

³ Guizhou Bureau of Geology and Mineral Exploration and Development, Guiyang 550003, China; 103zq@163.com

⁴ No.103 Geological Party, Guizhou Bureau of Geology and Mineral Exploration and Development, Tongren 554300, China; jedxavier30@126.com

* Correspondence: shanxu0919@gmail.com



Citation: Gao, L.; Xu, S.; Hu, X.; Liu, S.; Zhou, Q.; Yang, B. Sedimentary Setting and Ore-Forming Model in the Songtao Manganese Deposit, Southwestern China: Evidence from Audio-Frequency Magnetotelluric and Gravity Data. *Minerals* **2021**, *11*, 1273. <https://doi.org/10.3390/min11111273>

Academic Editor: António Manuel Nunes Mateus

Received: 6 October 2021

Accepted: 15 November 2021

Published: 17 November 2021

Publisher's Note: MDPI stays neutral with regard to jurisdictional claims in published maps and institutional affiliations.



Copyright: © 2021 by the authors. Licensee MDPI, Basel, Switzerland. This article is an open access article distributed under the terms and conditions of the Creative Commons Attribution (CC BY) license (<https://creativecommons.org/licenses/by/4.0/>).

Abstract: The break-up of the supercontinent Rodinia in the late Neoproterozoic led to the formation of the Nanhua rift basin within the South China Block. The Datangpo-type manganese deposit, which developed in the Nanhua rift basin, is one of the most important types of manganese deposits in South China. Although it is widely accepted that deep sedimentary structures significantly affect the manganese ore system, the relationship between the manganese deposits in South China and the Nanhua rifting process is still unclear. The origin of the manganese ore layer remains controversial. In this paper, we integrated the audio-frequency magnetotelluric (AMT) data, gravity data, and comprehensive geological and borehole data analysis to characterize the structure of the Datangpo-type manganese deposit in Songtao, Guizhou Province. The resistivity and density models produced an inclined layered structure, which correlated well with the coeval sediment strata of the Nanhua rift basin. A high-resistivity cap was observed from the surface to a depth of 800 m, corresponding to the Cambrian Loushanguan (ϵ_{3-4ls}) and Palang dolomite formation (ϵ_{2p}), which has helped the storage of the manganese ore. The most significant low-resistivity anomaly (25–40 Ω -m) resides at a depth of 1400 m in the Nantuo (Nh_{3n}) gravel sandstone and Datangpo (Nh_{2d}) silty and carbonaceous shale, corresponding to the ore-forming layer. This distinct low-resistivity layer was possibly produced by aqueous fluids and pyrite in the syn-sedimentary fault and alteration zone. The accumulations of sulfide minerals in the rock samples suggest a possible anoxic-euxinic deposition environment during the manganese mineralization and precipitation. The fault revealed in the resistivity models is perhaps a previous fault zone produced by extension in the Nanhua rifting process, which provided migration and upwelling channels for ore-forming minerals. Based on our resistivity models, density models, and geological survey, the manganese ore-forming model was derived, which can help to provide geophysical evidence for the origin of the Datangpo-type manganese deposit.

Keywords: manganese ore deposit; audio-frequency magnetotellurics; gravity; mineral exploration

1. Introduction

The break-up of Rodinia began around 750 Ma and led to rift systems on the margins of Laurentia, Australia, and the Yangtze Block [1]. Two of the best-documented rift basins are the north–south trending failed rift in western Sichuan (the Kangdian rift), and the basin between the southeastern Yangtze Block and northwestern Cathaysia Block (the Nanhua rift) [2]. Manganese deposits in the lower Sinian (664–653 Ma) Datangpo formation (Nh_{2d}) of the Nanhua rift are known as “Datangpo-type”. The Songtao area in Guizhou (Figure 1a) hosts the most important Datangpo-type manganese deposits, the greatest manganese

resource potential in China [3]. Additionally, in these deposits, the Gaudi deposit (Figure 1b) has the highest manganese grade of 160,906,000 tons and reaches the grade of super-large deposits [4]. The Datangpo manganese ore layer, located at depths below 1000 m, primarily consists of manganese carbonates (rhodochrosite) and manganese-bearing aluminosilicates. Manganese mineralization mainly occurs along syn-sedimentary faults, which developed in an extensional tectonic setting in the Nanhua rift during the break-up of Rodinia. In the late Neoproterozoic, the syn-sedimentary faults and secondary rift basins might have facilitated mineral transportation. Therefore, the subsurface structure of the mineralization system needs to be resolved.

The exploration of the manganese deposit in the Songtao area started in the 1980s and included a number of studies of paleogeography, lithology, geochemistry, and sedimentary environment analysis. Despite the long mining history of subaerial manganese ore in this area, the origin of the manganese ore layer remains controversial. There are two opposing models. On the one hand, the hydrothermal genetic model suggested by Xu et al. [5] indicated that the manganese deposit originated from hydrothermal activity based on the concentrically layered modular structure and coliform texture of the ore. The large-scale submarine volcanic and hydrothermal activity might have been triggered due to strong crustal extension and rifting processes during the break-up of Rodinia. Thus, the manganese and products during volcanic eruption rapidly accumulated into manganese-containing tuffaceous sediments [6]. The volcanic-derived gas–liquid and heated seawater further dissolved and filtered these loose sediments, which led to the enrichment and deposition of manganese in the aulacogens. On the other hand, a shallow-water genetic model was inferred instead, considering that the REE patterns in the manganese deposit are not characteristic of hydrothermal influence [7]. Zhao [8] proposed that the “Datangpo-type” rhodochrosites consist of debris and carbon argillaceous composition. Additionally, the “Datangpo-type” deposits form in a shallow-water sedimentary environment and flow into deep water along the basin slope. The manganese ore has graded bedding and turbidite sedimentary characteristics due to this sedimentary process. The shallow-water genetic model was supported by low contents of Si, Ba, Fe, and Sr, and high values of Ti and Al in the manganese ore [9]. Yang et al. [10] studied the carbon and sulfur isotopes of Songtao manganese deposits and found that the deep faults and fluids in this area have provided a large amount of Mn^{2+} , whereas the CO_2 that helped to produce $MnCO_3$ originated from the high volume of CO_2 in the atmosphere after the global Sturtian ice age in 700–695 Ma. In addition, Zhou et al. [11] discovered a large number of ancient leakage structures of natural gas, with low carbon and extremely high contents of sulfur in the rhodochrosites, and a new model incorporating Neoproterozoic rifting and natural gas leakage was suggested [11–13]. However, this model has not yet been testified with any geophysical data.

To discriminate the metallogenic model of the Datangpo-type manganese ore, it is necessary to further study the deep structure of the mineralization system and the sedimentary setting. In this study, we utilized resistivity models derived from audio-frequency magnetotelluric (AMT) data (blue dots in Figure 1c) and a density model derived from gravity data (gray dotted line in Figure 1c) to reveal the regional tectonic structure and ore deposition settings in the Songtao manganese deposit, and by reference to study the manganese metallogenic model in South China. The geoelectrical model may provide information to understand the distribution of conducting phases, because magnetotelluric data are relatively sensitive to electrical conductors such as the sulfides and oxides of some minerals and coal/graphitized rocks (gneisses, schists, silts, and sandstones). The interpretation of resistivity and density models is constrained by borehole and geological data. The regional subsurface structure to a depth of 2800 m is delineated, potentially being beneficial for the further prospecting of other manganese deposits.

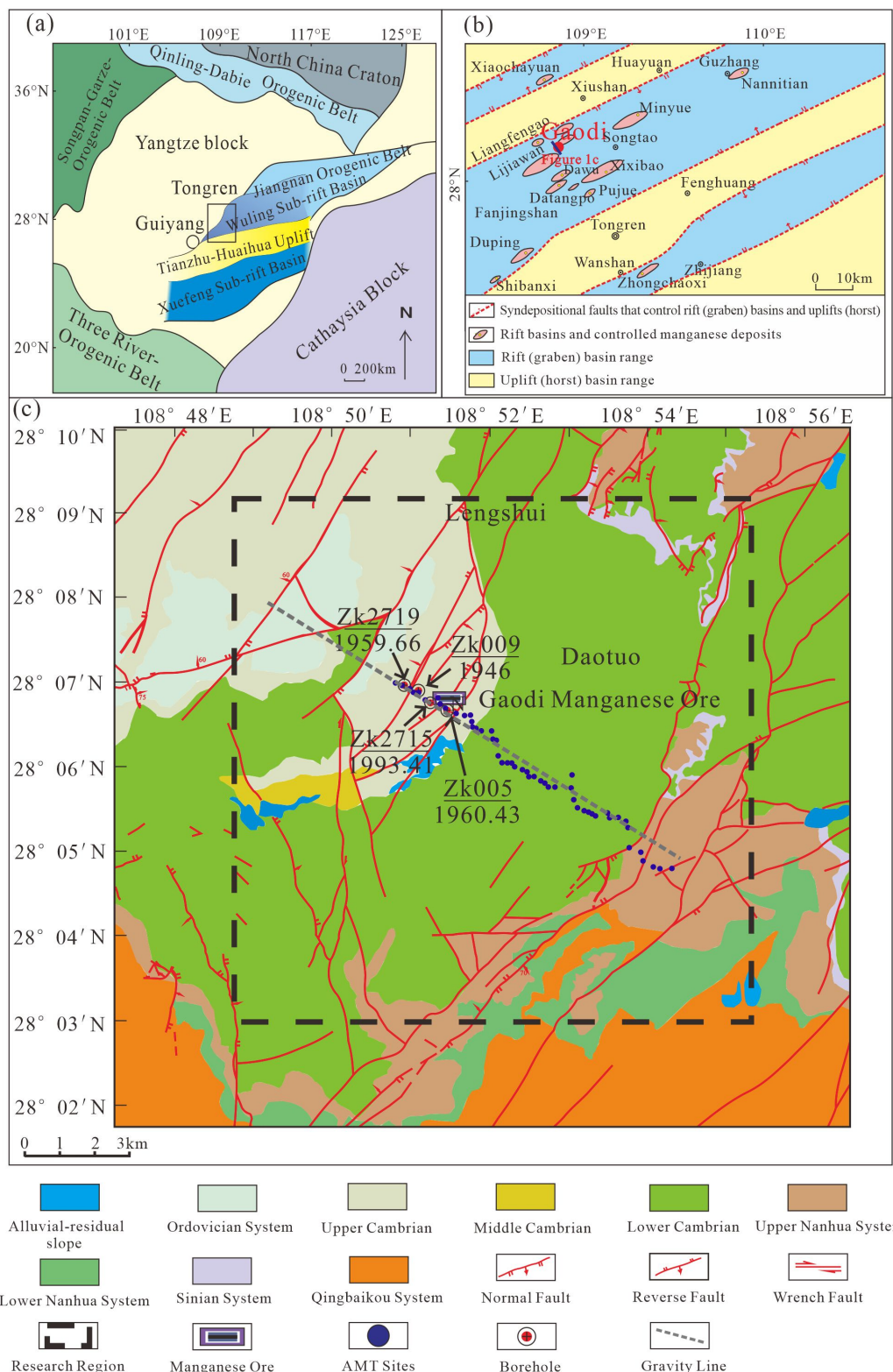


Figure 1. (a) Location and simplified geology map of the study area (redraw after [2]). The black boxes indicate the study area. (b) Subdivision of the Nanhua rift (modified after [13]). (c) Distribution map of the AMT stations and gravity stations. The black arrows point to the location of the boreholes.

2. Geological Background

The Songtao manganese deposit is located on the southeastern margin of the Yangtze Block. The break-up of the Rodinia supercontinent in 825–750 Ma led to the Nanhua rift

system in the South China Block [14,15]. The break-up process mainly occurred along the suture zone between the Yangtze and Cathaysia Blocks, and a series of secondary rift basins developed along the deep fault zones. Many world-class manganese deposits formed in this period [16–19]. The west section of the Nanhua rift basin comprises three tectonic units: the Wuling sub-rift basin in the north, Xuefeng sub-rift basin in the south, and the Tianzhuan–Huaihua uplift area in the middle. The Songtao manganese ore is located in the rifting center of the Wuling sub-rift basin [13]. Neoproterozoic and Paleozoic successions are divided into the Qingbaikou system, the Liangjiehe formation (Nh₁l), Tiesiao formation (Nh₂t), Datangpo formation (Nh₂d), and Nantuo formation (Nh₃n) of the Nanhua System, the Doushantuo formation (Z₁d), and Liuchapo formation (Z₁l) of the Sinian System, Jiumenchong formation (ε₂jm), Bianmachong formation (ε₂b) and Palang formation (ε₂p) of the Cambrian System, in ascending order. The Tiesiao formation (Nh₂t) and Nantuo formation (Nh₃n) are equivalent to the Sturtian and Marinoan glaciations, respectively [20–22]. The Datangpo formation (Nh₂d) can be subdivided into two strata. The lower stratum mainly consists of 0–20 m thickness of black carbonaceous shales, a carbonaceous rhodochrosite lens and lenticular dolomites. The upper stratum is 30–320 m thick and is mainly composed of gray to dark gray silty mudstones and siltstones. Sedimentary manganese mineralization in the late Neoproterozoic is the primary mineralization in this area, primarily occurring in rhodochrosite at the bottom of the black shale of the lower stratum of the Datangpo formation (Nh₂d). The ages of mineral deposition can be preliminarily determined from the U-Pb zircon ages of volcanic tuff samples at the bottom and top of Datangpo formation (Nh₂d) at 662.9 ± 4 Ma and 654.5 ± 3.8 Ma, respectively [20,23,24]. Notably, most of the manganese deposits in eastern Guizhou reside along syn-sedimentary faults that widely developed in the late Neoproterozoic. In South China, these faults accompanying the Rodinia break-up might have controlled the formation of secondary rift basins, and served as channels for the spillage of deep fluid and manganese material. Thus, the identification of syn-sedimentary faults may link the manganese formation and the Nanhua rifting processes.

3. Data

3.1. AMT Data Acquisition and Analysis

An NWW-trending profile with 51 broadband MT (with the frequency range from 10,400 Hz to 1 Hz) sites was deployed perpendicular to the geological strike direction (Figure 2), with a site spacing of 100–200 m using Phoenix V5-2000 instruments (Phoenix Geophysics Limited, Toronto, ON, Canada). Two orthogonal horizontal electric field components (Ex and Ey) and three orthogonal magnetic field components (Hx, Hy, Hz) were recorded at each site.

The time series data were processed with Phoenix SSMT2000 software (version 0.6.0.69, Phoenix Geophysics Limited, Toronto, ON, Canada). The AMT impedance tensor data were obtained after fast Fourier-transform and robust impedance tensor estimation processing. Data with frequencies lower than 1 Hz were eliminated to diminish electromagnetic noise. Some of the low-frequency data from the measurement points were even removed below 10 Hz. The power spectra corresponding to different frequencies of each site were evaluated. The depth of exploration depends on skin depth, which increases with the increase in the period. For this dataset, the longest period was 1 s, and it produces a skin depth of 2–3 km, assuming an average resistivity value of 100 Ω·m.

Before inversion, Bahr skewness (S) values of the AMT impedance data were calculated to determine the dimensionality [25]. This method can effectively avoid the effect of local distortion and obtain the dimensionality of the regional structure (Figure 2). The geoelectric strike direction was estimated for all sites at all frequencies. $S = 0$ indicates an ideal two-dimensional (2D) structure. In general, small S values indicate that the subsurface structure is more likely to be a two-dimensional structure. As shown in Figure 2a, at frequencies above 100 Hz, the Bahr skewness at most stations was less than 0.3. Thus, the electrical structure along the whole section was approximately two-dimensional in the

shallow part. However, larger skewness was observed at frequencies lower than 100 Hz, especially at stations in the western region, which may indicate a three-dimensional (3D) structure and require 3D inversion to recover the deep structure below these stations. Therefore, we used both 2D and 3D inversion techniques to obtain the resistivity structure along with the AMT profile.

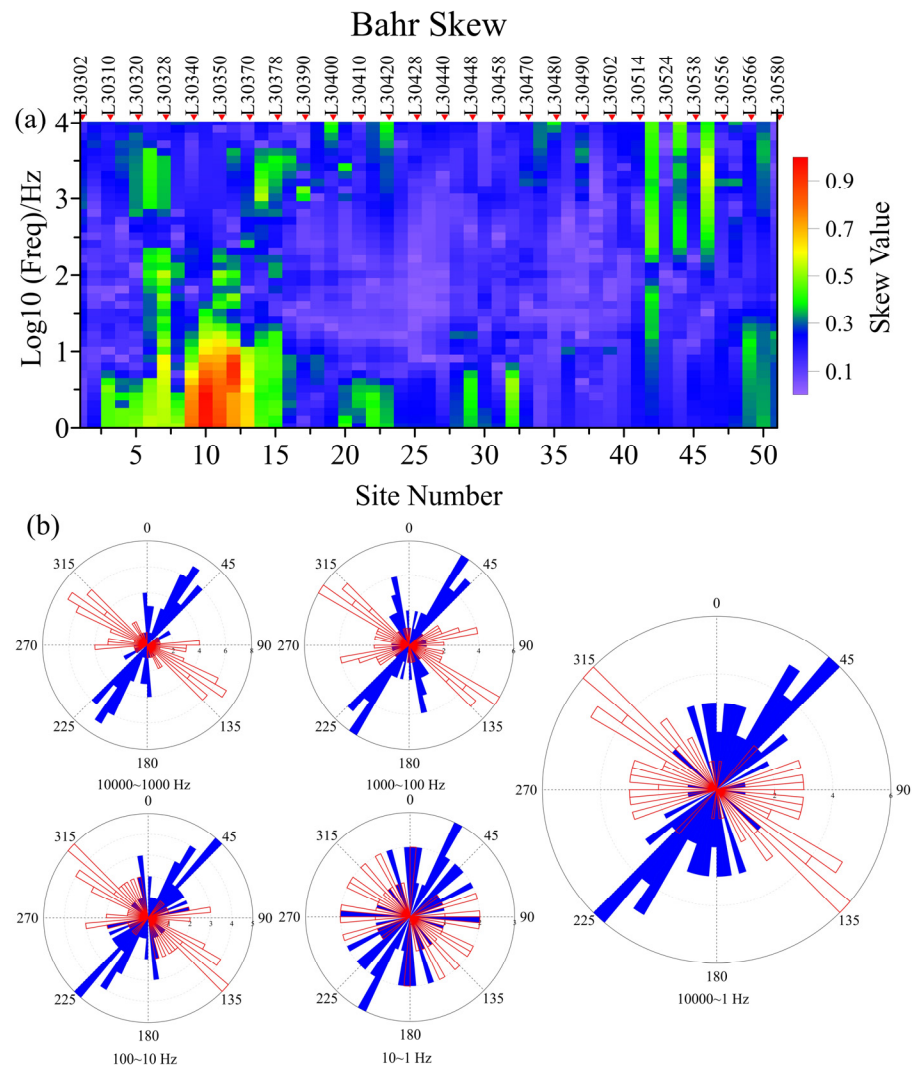


Figure 2. (a) Bahr skewness map, showing the deviation from 2D structure. (b) Rose diagrams drawn using multisite–multifrequency tensor decomposition method, which show the geoelectric strike direction at different frequency ranges.

The geoelectric strike direction should be determined before 2D inversion. Then, the AMT data need to be rotated to the geoelectric strike direction. The method of multi-site multi-frequency impedance decomposition was used [26–28]. According to the statistical results of the geoelectric directions in the rose diagrams (Figure 2b), the geoelectric strike direction of the middle and shallow depths (at 100–10,000 Hz) is about N40° E. The geoelectric strike direction in the deeper part (at frequencies of 1–100 Hz) changes significantly, suggesting that the dimensionality of the deeper structure tends to be 3D. Local variations of strike direction are all within a minimal range, consistent with the regional geological strike direction. Therefore, the electrical strike direction along this profile was determined to be N40° E.

3.2. Gravity Data Acquisition and Analysis

High-precision gravity measurements were implemented at the same profile of the AMT survey (Figure 1c). The gravity profile consisted of 259 survey points with an average point spacing of 40 m, and the length of the profile reached 10.52 km in total. A CG-5 (Scintrex, Concord, ON, Canada) gravimeter was used for the gravity measurements, and the observed precision of gravity data reached 0.016 mGal. For obtaining the Bouguer gravity anomaly, the gravity data observed need a series of corrections, including Earth tide correction, zero drift correction, free-air correction, stone slab correction, and topographic correction. Here, an average density of the stone slab, 2.67 g/cm^3 , was given for the Bouguer correction.

To remove the shallow and local field anomaly, we have implemented the separation of regional and local field data for the Bouguer gravity anomaly by using the moving window average method. Additionally, the window size was equal to 40 observation points (i.e., 1.6 km). Finally, the regional Bouguer gravity anomaly is shown in Section 4.3. The gravity anomaly value varied from 2 to 15 mGal. The gravity anomaly increased from northwest to the southeast with two regional high-amplitude gravity anomalies. The gravity anomaly was inverted to determine the density structure of the subsurface and interpreted with the geoelectrical model.

4. Geophysical Data Inversion and Interpretation

4.1. AMT Inversion

After rotating the AMT impedance data to the geoelectrical principal axis, 2D inversion was performed using the non-linear conjugate gradient method (NLCG) [29]. Previous studies have shown that Transverse Electric (TE) mode data are more sensitive to vertical variation in the resistivity structure, whereas the Transverse Magnetic (TM) mode is more sensitive to lateral changes [30]. To obtain the most reasonable 2D electrical structure, TE and TM joint mode inversion were conducted. After comparing different inversion parameters, the final inversion parameters were set using a $100 \text{ } \Omega \cdot \text{m}$ uniform half-space as the initial model. The trade-off parameter between model roughness and data fit was determined using an “L-curve” (Figure 3), which exhibited a gradient change when the regularization parameter was 7. Therefore, the optimal value of regularization was 7. After 100 iterations, the overall root mean square (RMS) value was 2.13, indicating that the inversion had already converged. The final 2D inversion model is shown in Figure 4a. The observed and model response curves of apparent resistivity and phase data for the 2D inversion of some stations are shown in Figure A1.

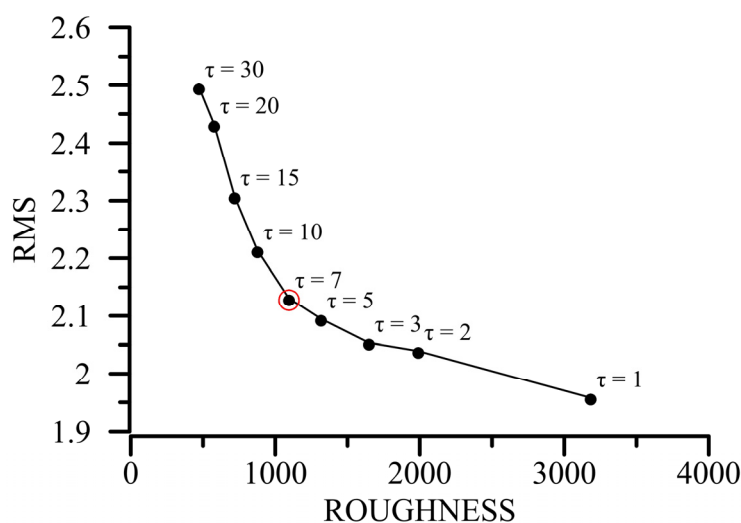


Figure 3. L-curve showing the variation in RMS values and model roughness when using different regularization parameters.

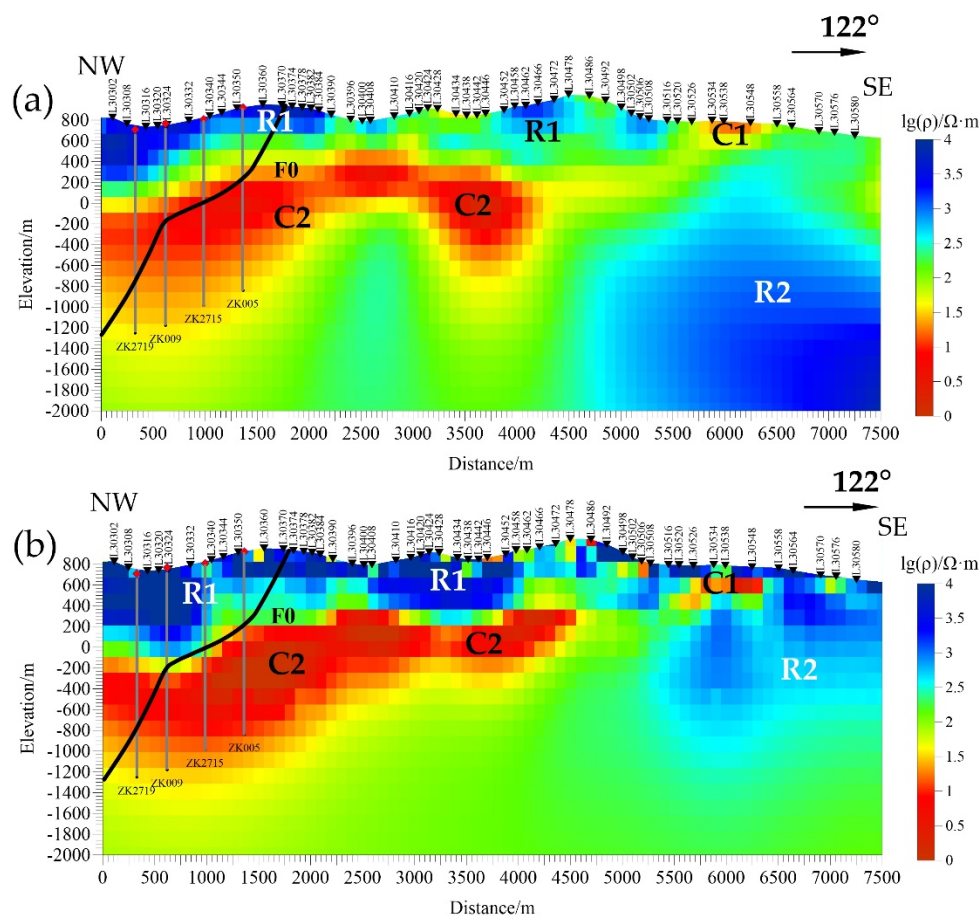


Figure 4. (a) The resistivity model of 2D inversion. (b) The resistivity model of 3D inversion. C1 and C2 denote conductors. R1 and R2 show resistors. The regional fault, F0, is indicated by a black line.

Three-dimensional inversion was applied to the AMT data at 51 stations. We used the Modular system for Electromagnetic Inversion (ModEM) for the 3D inversion [31,32]. This non-linear conjugate gradient inversion algorithm was run in parallel mode on a cluster with 67 processors. For each station, 20 frequencies in the range of 1–10,000 Hz were used. The model area was discretized with a grid that had 100 m horizontal spacing in the center, padded with eight cells on all edges, with width increasing by a factor of 1.3 outward to the boundary. In the vertical direction, 40 layers were used, starting with a thickness of 10 m and increasing geometrically with a factor of 1.3. This discretization resulted in a $58 \times 78 \times 47$ grid in the x , y , and z directions, respectively. The prior model was set to a $100 \Omega \cdot \text{m}$ half-space. We started from a $100 \Omega \cdot \text{m}$ half-space with topography and obtained the 3D resistivity model by inverting the full impedance tensor. A moderate error floor of $10\% \text{ of } |Z_{xy}Z_{yx}|^{1/2}$ was assigned to all four components of the impedance tensor. The resistivity models obtained after 138 iterations were used as the final 3D model (Figure 4b), which fitted the measured AMT data with a normalized RMS misfit of 1.64. The observed and model response curves of impedance tensor for the 2D inversion of some stations are shown in Figure A2.

4.2. Electrical Resistivity Structure

A comparison of the preferred 2D and 3D inversion models is shown in Figure 4, exhibiting similar resistivity features. It indicates that the resistivity features in the 2D and 3D models were very robust. The high-resistivity formations of over $2000 \Omega \cdot \text{m}$ (R1) at depths less than 800 m correspond to the Cambrian Loushanguan formation (ϵ_{3-4} ls) and the Cambrian Palang formation (ϵ_{2p}), as determined from the borehole (Figure 5), which

comprised dolomite and calcareous sandstone. Below the high-resistivity feature R1, a continuous layer of moderate resistivity (300–1000 Ω·m) was revealed at the Cambrian Bianmachong formation (ϵ_2b) and Doushantuo formation (Z_1d). This layer comprised calcareous sandstone and siltstone, with thin sheets of siliceous rocks and dolomite (Table 1). The high-resistivity body R2 in the east could have been caused by basement uplift.

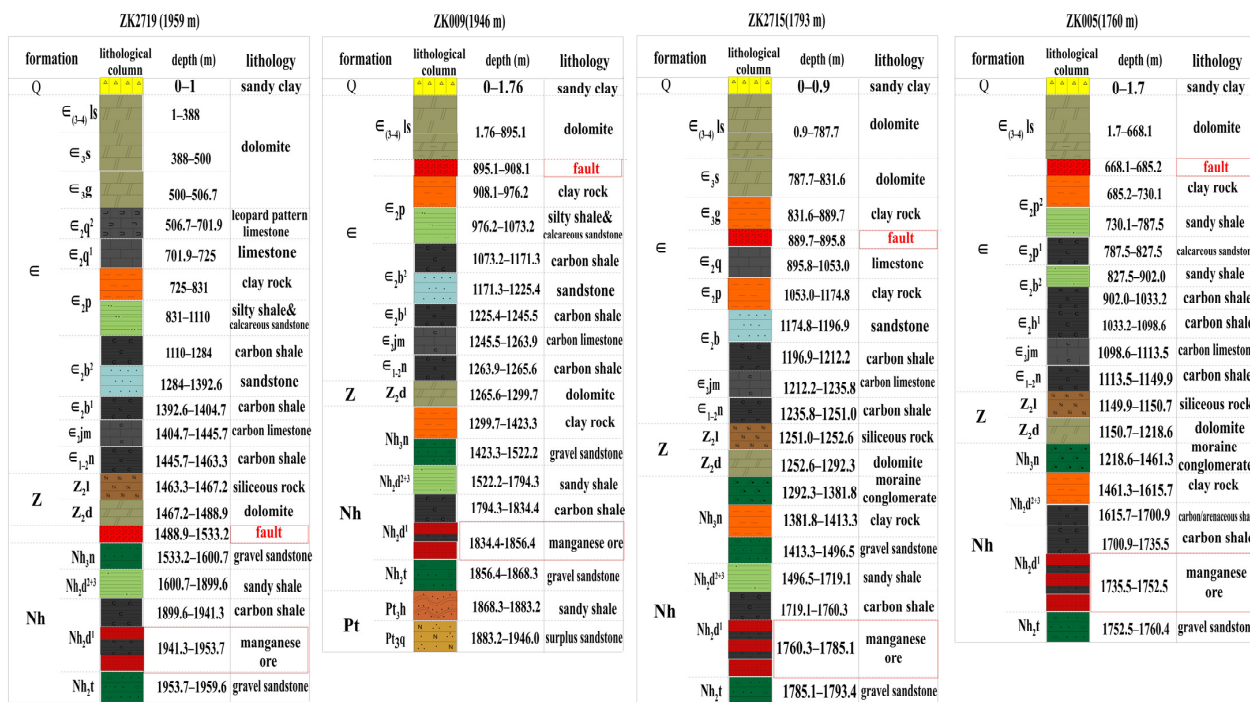


Figure 5. Lithological column and formation thickness at 4 boreholes. The banded black and red formations indicate carbon shale containing manganese ore layers.

Table 1. Resistivity of rock samples in the study area (the rock samples were collected from the borehole rocks in Figure A3).

Rock Type	Lithology	Sample Number	Average Resistivity (Ω·m)	Average Density (g/cm ³)
dolomite	$\epsilon_{3-4}ls, \epsilon_2q^{3+4}$	30	2508.71	2.79
limestone	ϵ_2q^{1+2}	38	4579.28	2.91
siliceous rock	Z_2l	33	4050.97	2.48
calcareous sandstone and siltstone	$\epsilon_2p, \epsilon_2b, Z_1d$	29	1614.33	2.55
gravel sandstone and moraine conglomerate	Nh_3n, Nh_2t	16	1732.58	2.84
carbonaceous shale	Nh_2d^2	36	26.22	2.58
silty shale	Nh_2d^2	22	551.35	2.62

Several small groups of low resistivity were resolved at the subsurface in the eastern portion of the profile (C1), which could be attributed to clay minerals. The most significant resistivity anomaly (C2) appeared at the northwest end of the profile at a depth of 1200 m and extended eastwards before it reached another resistive body, R2, at the southeastern end of the profile. The conductor C2 exhibits folded characteristic and rises gradually in the southeast, indicative of a sedimentary feature at the basin margin. Considering the lithology distribution revealed by the four boreholes (Figure 5), the underlying low-resistivity layer C2 could be inferred to be the Tiesiao formation (Nh_2t) and Datangpo formation (Nh_2d), the main components of which are gravel sandstone, silty shale, and

carbonaceous shale. According to the information from the four boreholes (Figure 5), there is a fault (F0 in Figure 4) within the low-resistivity zone C2, and the fracture zone of the fault is more than 10 m wide. The west and east sections of the profile have very different electrical structural characteristics. The depth of the bottom interface of the low-resistivity layer changed suddenly, perhaps reflecting the locations of the graben and horst. A set of pebbly sandstone and shale was revealed at depths of 1100–1950 m beneath stations L30308 to L30360, and it can be inferred that the low-resistivity layer was widely developed in the western portion of the study area. Notably, in the southeast of the profile, a set of high-resistivity layers with stepped distribution had developed under the intermediate resistivity layer. As noted above (Figure 1), the Lower Nanhua System is exposed in the southeast region of the study area, and large-scale overburden formation to the west of the survey line is exposed on the surface to the east of the survey line. In general, the Cambrian Loushanguan formation ($\epsilon_{3-4}ls$) to the Lower Cambrian Palang formation (ϵ_2p) is of relatively high resistivity; the Cambrian Bianmachong formation (ϵ_2b) to Sinian Doushantuo formation (Z_1d) are of relatively medium, and high resistivity; the Nantuo formation (Nh_3n) and Datangpo formation (Nh_2d) are of low resistivity; and the underlying basement is of relatively high resistivity. Therefore, the Songtao deposit demonstrates a three-layer resistivity structure, corresponding to the sedimentary setting in the Nanhua rift system.

4.3. Gravity Data Inversion

We use the 2D interactive inversion method [33] to invert the gravity anomaly in Figure 6a. In interactive inversion, the densities and shapes of the stratum are repeatedly revised to fit the gravity data. Thus, the advantages of interactive inversion are that we can use some prior information. In this study, we built the density model based on the borehole information of ZK2719, ZK009, ZK2715, and ZK005 and density measurement results in Table 1. The gravity anomaly inversion results are shown in Figure 6b. The data predicted by the density model accurately fitted the observed data with a fitting error of 6.6%.

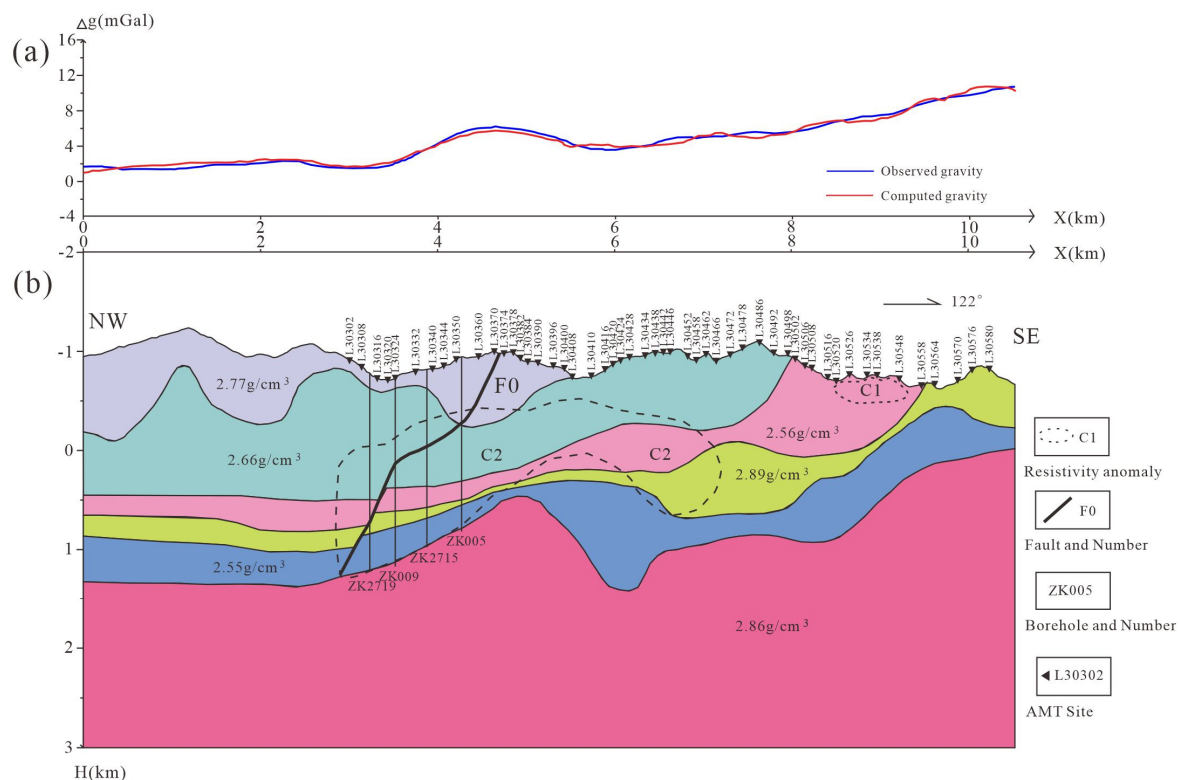


Figure 6. (a) Observed gravity curve and computed gravity curve. (b) The gravity density model of 2D interactive inversion.

deposits. In the Datangpo Period of the Wuling secondary rift basin, there were mainly two types of sedimentary facies: secondary rift (graben) basin facies and secondary uplift (horst) facies. In the grade basin, Liangjiehe formations (Nh₁l) are distributed, whereas in the underlying strata outside the grade basin, Liangjiehe formations (Nh₁l) are absent, and the underlying Tiesiao formation (Nh₂t) is in direct contact with the basement [13]. In the Gaodi area, the manganese deposit is located at a depth below 1500 m, verified by four boreholes on the west side of the survey line, and the Cambrian strata are widely exposed in the northwest of the depression. There were discrepancies in some thin formations in the borehole logs, perhaps as a result of tectonic evolution. In the borehole samples, there were obvious fracture and thickness changes in some strata samples, which are presumed to have been caused by faults (Figure 5). In the electrical profiles, a laterally continuous low-resistivity layer (C2) developed in the Nantuo formation (Nh₃n) and Datangpo formation (Nh₂d), whose burial depth gradually decreases in the eastern part of the section. The density model also showed clear stratification and the same trend. The regional geological survey showed that the Gaodi–Daotuo graben basin is long and narrow. The central strike of the graben basin is approximately in an NE–SW direction and the Gaodi super-large manganese deposit is located in the central part of the graben basin. As already stated, the southeastern portion of the profile is characterized by high resistivity (R2). On the east side of the density structure, the basement also shows obvious uplift. If R2 is considered as an uplift area from east to west, and the inversion models fit the measured geological data, possibly indicating that the syncline structure of graben and uplift of horst in the study area were formed under the compression stress from east to west. The density structure model reveals that the bedrock in the middle of the survey line shows a feature of uplift, and the strata ascending from the central basement uplift shows a change in thickness from NW to SE. The lithology of manganese-bearing rock series in the study area is a relatively weak zone, which plays a role in slippage adjustment in the process of structural deformation, adjusts folds formed by overlying strata, and controls the formation of the syncline.

The manganese-bearing rock series may have acted as a weak detachment layer, slipped and accumulated toward the core of the syncline, enriching it at the core of the syncline [35]. We synthesized resistivity and density models, and the study area shows a tectonic framework in which a depression is compressed by an uplift (Figures 4 and 6). At the bottom of the low-resistivity layer (C2), the resistivity of the manganese-bearing strata was between 25 Ω·m and 40 Ω·m. This layer is bounded by a high-resistivity cap (R1) in the shallow part, which helps the storage of the manganese ore. Syn-sedimentary faults were well-developed in the early Nanhua Period in the study area, controlling and forming secondary rift basins of different orders in the early Nanhua Period. The low-resistivity layer (C2) exhibited a dipping feature at the margin of the basin, which was presumed to indicate the existence of an ancient syn-sedimentary fault (F0 in Figure 4). This syn-sedimentary fault could have directly influenced the formation of ore deposits, controlling the shape, distribution, and accumulation of manganese, and providing the migration and upwelling channels of ore-forming minerals.

According to the borehole data and geological survey, the main composition of the manganese ore-forming body was rhodochrosite (manganese carbonate) with a dolomite lens. Dolomite mounds are scattered in clastic rocks and are considered as one of the typical signs of ancient methane leakage structures [36,37]. Cap carbonates are widely associated with manganese-rich deposits [38,39]. Some scholars believe that the manganese-rich carbonate layer at the bottom of the Datangpo formation (Nh₂d) is equivalent to the carbonate cap layer [20,40,41]. Sturtian cap carbonates in the Nanhua Basin were deposited in shallow horsts, coeval with the manganese ore-forming basin (graben) [38,42]. In our resistivity models, the cap carbonates were most likely located above the low-resistivity layer, C2, whereas C2 was possibly produced by aqueous fluids and pyrite minerals in F0, as suggested by the low density revealed by our gravity data and high sulfur content in the rock samples. The accumulations of sulfide minerals in the samples also suggest a possible anoxic–euxinic deposition environment during manganese mineralization and

precipitation. The cap carbonate formation model proposed that a large amount of methane had been released globally, leading to the end of the snowball earth ice age [43–46]. The release of natural gas from the ancient syn-sedimentary fault F0 could explain the pores filled with asphalt in the rhodochrosite ore body of the Datangpo formation (Nh₂d) [11]. Therefore, the formation of manganese ore has a close relationship with natural gas leakage in the Datangpo formation (Nh₂d) at the end of the snowball earth ice age [11]. With the arrival of the interglacial period, the temperature gradually warmed up, the original natural gas hydrate gasified and leaked upward, and organic matter accumulated in Datangpo formation (Nh₂d). At the same time, microorganisms using methane as an energy source develop and can form microbial mats and microbial mounds. Therefore, the dark shale of Datangpo formation (Nh₂d) is also a potential high-quality hydrocarbon source rock. The density model revealed by gravity data can also prove that the stratigraphic environment provided good manganese deposition and enrichment conditions. Mineralogical characteristics, geochemical environment, and the influence of microbial hydrocarbon source rocks suggest that the vertical development of syn-sedimentary fault (F0) has formed manganese ore-forming channels. The low-resistivity body at the bottom of the manganese-forming basin in the study area is the spout where the manganese-rich fluid overflows and the place where manganese ore deposits. Based on the above deductions, a genetic ore-forming model is derived in Figure 8. The element characteristics of Datangpo formation (Nh₂d) reflect that the source of manganese carbonate is mainly a hydrothermal source [38]. The fault zones produced by the extension in the Nanhua rifting process acted as the primary transportation system of hydrothermal fluids. The manganese carbonate deposition resulted from reactions between aqueous manganese and sedimentary organic matter during early diagenesis. Additionally, it led to elevated Mn²⁺ concentrations and alkalinity in sediment porewaters, as suggested by geochemical analysis [38]. These faults may also have been activated by later tectonic activities. A series of uplifts and depressions in Nanhua Rift Basin all indicate that the migration channel of Datangpo ore-forming minerals is related to previous deep faults.

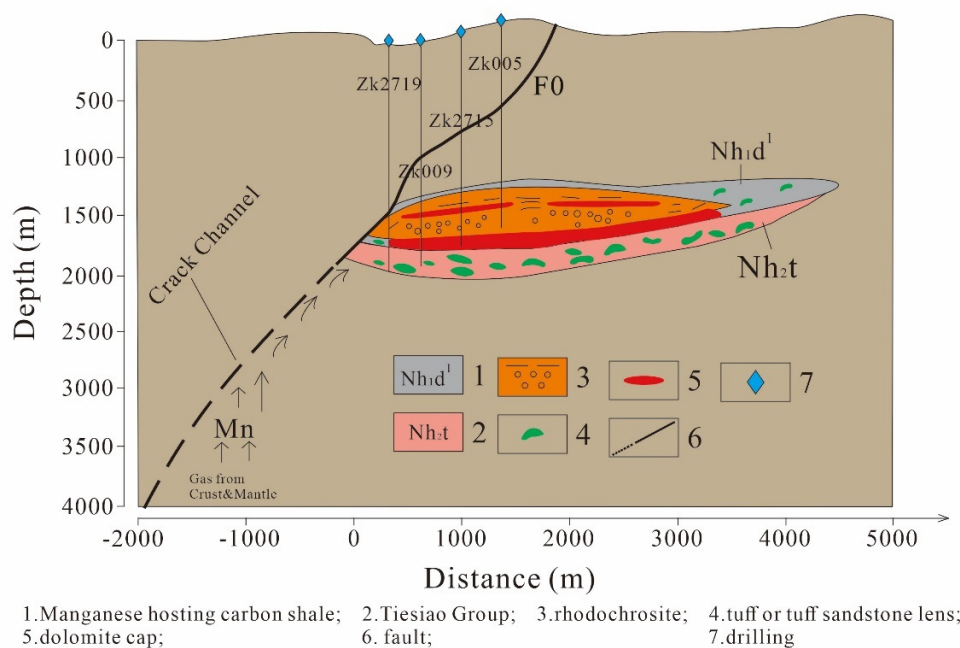


Figure 8. Metallogenesis model for the Datangpo manganese ore deposit. Arrows represent potential transport routes for manganese from deep to shallow.

6. Conclusions

Based on the geological and geophysical models, the genetic model was derived to explain the formation of the “Datangpo-type” manganese ore. Our resistivity models

discovered a low-resistivity anomaly ($25\text{--}40 \Omega\cdot\text{m}$) that resided at a depth of 1200 m in the Nantuo formation (Nh_3n) and Datangpo formation (Nh_2d), corresponding to the manganese-ore-forming layer. The manganese-ore-forming layer was near the interface between low-density layer and basement in the density model. This distinct low-resistivity layer was possibly produced by aqueous fluids and pyrite minerals in F0. The low-resistivity layer and the stratification of our density model showed a dipping feature at the margin of the basin, which is presumed to facilitate the accumulation of manganese. The enriched accumulation of sulfide minerals in the rock samples suggests a possible anoxic-euxinic deposition environment during the manganese mineralization and precipitation. The F0 fault zone revealed in our resistivity models is perhaps a previous fault zone produced by the extension in the Nanhua rifting process, which has directly influenced the formation of ore deposits, controlled the shape, distribution and accumulation of manganese, and provided the migration and upwelling channels for ore-forming minerals. Finally, our study supports a hydrothermal genetic model. The fracture fault zones acted as the primary transportation system of hydrothermal fluids. The manganese carbonate deposition was the result of reactions between aqueous manganese and sedimentary organic matter during early diagenesis that led to elevated Mn^{2+} concentrations. A high-resistivity cap bound the ore-forming layer at the subsurface, which helps the storage of the manganese ore.

Author Contributions: Conceptualization, L.G.; methodology, L.G. and S.X.; validation, S.X.; formal analysis, S.L.; resources, X.H.; data curation, L.G. and S.L.; S.L.; writing—original draft preparation, L.G. and S.X.; writing—review and editing, S.X. and S.L.; project administration, X.H. and B.Y.; supervision, Q.Z. All authors have read and agreed to the published version of the manuscript.

Funding: This work is supported by the Science and Technology Program of Guizhou Province (No. [2019] 2868 and No. 2019 [2]), the National Natural Science Foundation of China (No. 42004062; U1812405) and MOST Special Fund from the State Key Laboratory of Geological Processes and Mineral Resources, China University of Geosciences No. MSFGPMR01-4.

Data Availability Statement: Not applicable.

Acknowledgments: This manuscript greatly benefited from the valuable comments and suggestions from the anonymous reviewers and editors of Minerals.

Conflicts of Interest: The authors declare no conflict of interest.

Appendix A

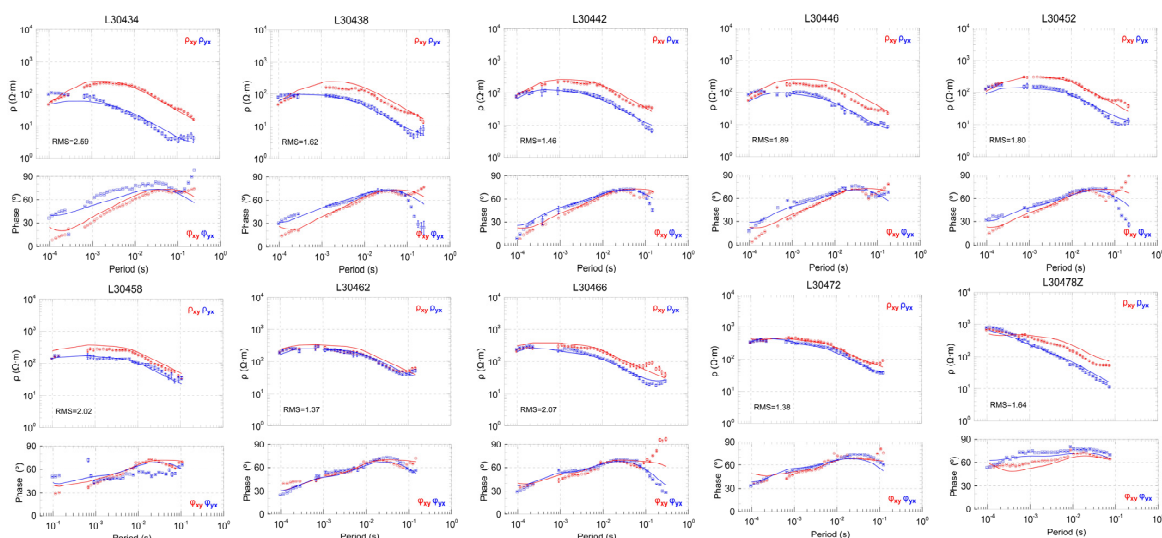


Figure A1. Observed and model response curves of apparent resistivity and phase data for the 2D inversion. The solid curves denote model responses. Small “T” signs emerging from dots on graph represent error bars.

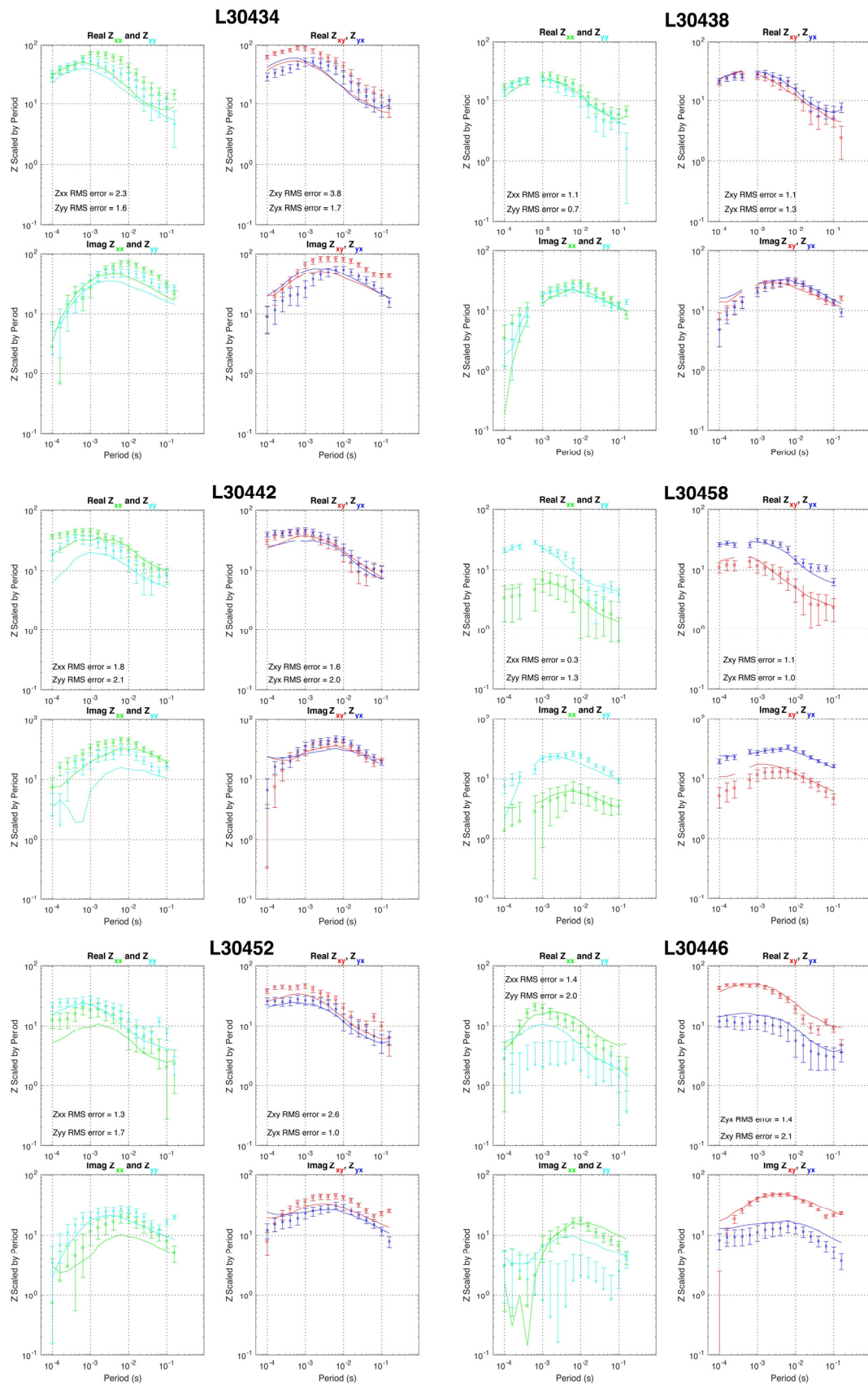


Figure A2. Cont.

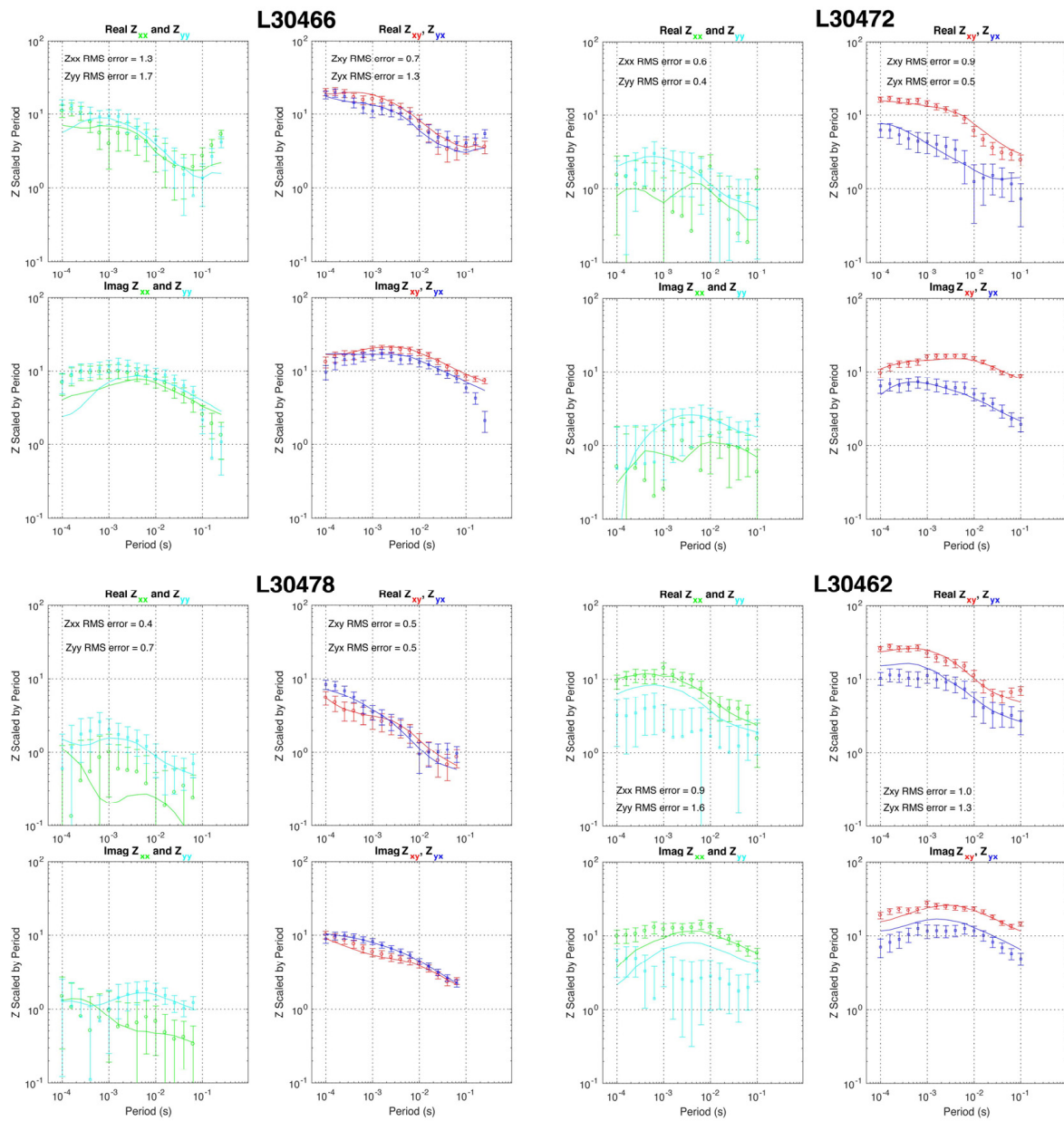


Figure A2. The observed and model response curves of apparent resistivity and phase data for the 3D inversion. The solid curves denote model responses. Small “T” signs emerging from dots on graph represent error bars.

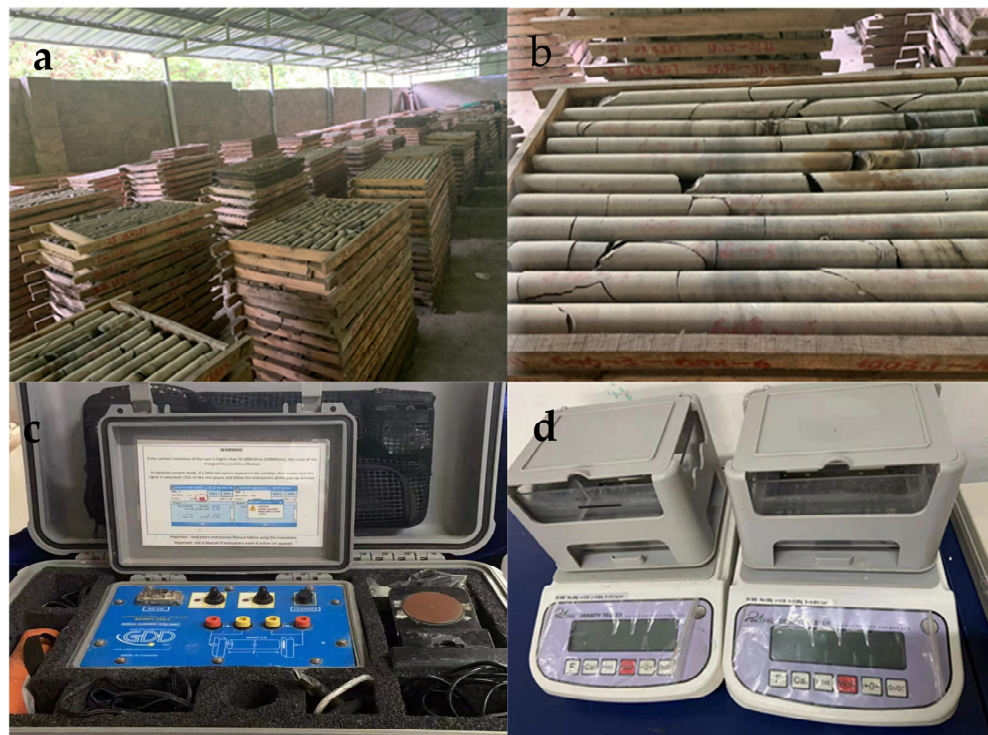


Figure A3. (a) Borehole sample collection; (b) partial borehole sample; (c) resistivity test equipment (SCIP); (d) density measuring equipment (DX-300Z).

References

1. Zhao, G.; Wang, Y.; Huang, B.; Dong, Y.; Li, S.; Zhang, G.; Yu, S. Geological reconstructions of the East Asian blocks: From the breakup of Rodinia to the assembly of Pangea. *Earth-Sci. Rev.* **2018**, *186*, 262–286. [[CrossRef](#)]
2. Wang, J.; Li, Z.-X. History of Neoproterozoic rift basins in South China: Implications for Rodinia Break-up. *Precambrian Res.* **2003**, *122*, 141–158. [[CrossRef](#)]
3. Zhou, Q.; Du, Y.S.; Yuan, L.J.; Zhang, S.; Yu, W.C.; Xie, X.F.; Yang, B.N. Research History, Major Progress and Outlook of ‘Datangpo Type’ Manganese Deposit in Nanhua Period of East Guizhou and Nearby Area. *Guizhou Geol.* **2018**, *35*, 270–281. (In Chinese with English Abstract)
4. Yuan, L.J.; Xie, X.F.; Yang, B.N.; Xie, X.Y.; Liu, J.; Shen, X.Q.; Zhao, F.Q. *A Sub-Project Report of Mineral Investigation and Prospecting Prediction in the Integrated Exploration Area of Tongren Songtao Manganese Mine in Guizhou Province*; No.103 Geological Party; Guizhou Bureau of Geology and Mineral Exploration and Development: Guizhou, China, 2019. (In Chinese)
5. Xu, X.; Huang, H.; Liu, B. Manganese Deposits of the Proterozoic Datangpo Formation, South China: Genesis and Palaeogeography. In *Sediment-Hosted Mineral Deposits: Proceedings of a Symposium Held in Beijing, People’s Republic of China, 30 July–4 August 1988*; Blackwell Publishing Ltd.: Oxford, UK, 1990; pp. 39–49.
6. Yang, S.; Lao, K. Study on Metallogenic Model of Manganese Deposit in Northwest Hunan—Take the Minle Manganese Deposit in Huayuan, Hunan Province as an example. *Sediment. Geol. Tethyan Geol.* **2006**, *26*, 72–80. (In Chinese with English Abstract)
7. Tie-bing, L.; Maynard, J.B.; Alten, J.; Kesler, S.E.; Ohmoto, H. Superheavy S isotopes from glacier-associated sediments of the Neoproterozoic of south China: Oceanic anoxia or sulfate limitation? In *Evolution of Early Earth’s Atmosphere, Hydrosphere, and Biosphere—Constraints from Ore Deposits*; Geological Society of America: Boulder, CO, USA, 2006.
8. Zhao, D. Intraclastic structures and gravity flow sedimentation of rhodochrosite ore in sinian Datangpo Formation. *Chin. J. Geol.* **1990**, *2*, 149–157. (In Chinese with English Abstract)
9. Chen, D.; Chen, X. Geological and Geochemical Characteristics of Songtan Hydrothermal Sedimentary Manganese Deposits, Guizhuo. *Acta Sedimentol. Sin.* **1992**, *10*, 35–43. (In Chinese with English Abstract)
10. Yang, R.; Ouyang, Z.; Zhu, L.; Wang, S.; Jiang, L.; Zhang, W.; Gao, H. A new understanding of manganese carbonate deposits in early Sinian Datangpo Stage. *Acta Mineral. Sin.* **2002**, *22*, 34–39. (In Chinese with English Abstract)
11. Zhou, Q.; Du, Y.S.; Wang, J.S.; Peng, J.Q. Characteristics and Significance of the Cold Seep Carbonates from the Datangpo Formation of the Nanhua Series in the Northeast Guizhou. *Earth Sci.* **2007**, *32*, 339–346. (In Chinese with English Abstract)
12. Zhou, Q.; Qin, Y. Ancient natural gas seepage sedimentary-type manganese metallogenic system and ore-forming model: A case study of Datangpo type’ manganese deposits formed in rift basin of Nanhua Period along Guizhou-Hunan-Chongqing border area. *Miner. Depos.* **2013**, *32*, 3–12. (In Chinese with English Abstract)

13. Zhou, Q.; Du, Y.S.; Yuan, L.J.; Zhang, S.; Yu, W.C.; Yang, S.T.; Liu, Y. The Structure of the Wuling Rift Basin and Its Control on the Manganese Deposit during the Nanhua Period in Guizhou-Hunan-Chongqing Border Area, South China. *Earth Sci.* **2016**, *41*, 177–188. (In Chinese with English Abstract)
14. Li, Z.X.; Li, X.H.; Kinny, P.D.; Wang, J.; Zhang, S.; Zhou, H. Geochronology of Neoproterozoic syn-rift magmatism in the Yangtze Craton, South China and correlations with other continents: Evidence for a mantle superplume that broke up Rodinia. *Precambrian Res.* **2003**, *122*, 85–109. [[CrossRef](#)]
15. Li, Z.X.; Bogdanova, S.V.; Collins, A.S.; Davidson, A.; De Waele, B.; Ernst, R.E.; Fitzsimons, I.C.W.; Fuck, R.A.; Gladkochub, D.P.; Jacobs, J.; et al. Assembly, configuration, and break-up history of Rodinia: A synthesis. *Precambrian Res.* **2008**, *160*, 179–210. [[CrossRef](#)]
16. Gutzmer, J.; Beukes, N.J. The manganese formation of the Neoproterozoic Penganga Group, India; revision of an enigma. *Econ. Geol.* **1998**, *93*, 1091–1102. [[CrossRef](#)]
17. Trompette, R.; Alvarenga, C.; Walde, D. Geological evolution of the Neoproterozoic Corumbágraben system (Brazil). Depositional context of the stratified Fe and Mn ores of the Jacadigo Group. *J. S. Am. Earth Sci.* **1998**, *11*, 587–597. [[CrossRef](#)]
18. Roy, S. Sedimentary manganese metallogenesis in response to the evolution of the Earth system. *Earth-Sci. Rev.* **2006**, *77*, 273–305. [[CrossRef](#)]
19. Maynard, J. The Chemistry of Manganese Ores through Time: A Signal of Increasing Diversity of Earth-Surface Environments. *Econ. Geol.* **2010**, *105*, 535–552. [[CrossRef](#)]
20. Zhou, C.M.; Tucker, R.; Xiao, S.H.; Peng, Z.X.; Yuan, X.L.; Chen, Z. New constraints on the ages of Neoproterozoic glaciations in south China. *Geology* **2004**, *32*, 437. [[CrossRef](#)]
21. Zhang, S.; Jiang, G.; Song, B.; Kennedy, M.; Christie-Blick, N. U-Pb sensitive high-resolution ion microprobe ages from the Doushantuo Formation in south China: Constraints on late Neoproterozoic glaciations. *Geology* **2005**, *33*, 473–476. [[CrossRef](#)]
22. Yin, C.Y.; Wang, Y.G.; Feng, T.; Wang, Z.Q.; Liu, P.J. SHRIMP II U-Pb zircon date from the Nanhuan Datangpo Formation in Songtao County, Guizhou Province. *Acta Geol. Sin.* **2006**, *80*, 273–278. (In Chinese with English Abstract)
23. Zhang, S.; Jiang, G.; Han, Y. The age of the Nantuo Formation and Nantuo glaciation in South China. *Terra Nova* **2008**, *20*, 289–294. [[CrossRef](#)]
24. Bao, X.; Zhang, S.; Jiang, G.; Wu, H.; Li, H.; Wang, X.; An, Z.; Yang, T. Cyclostratigraphic constraints on the duration of the Datangpo Formation and the onset age of the Nantuo (Marinoan) glaciation in South China. *Earth Planet. Sci. Lett.* **2018**, *483*, 52–63. [[CrossRef](#)]
25. Bahr, K. Geological noise in magnetotelluric data: A classification of distortion types. *Phys. Earth Planet. Inter.* **1991**, *66*, 24–38. [[CrossRef](#)]
26. Groom, R.W.; Bailey, R.C. Decomposition of magnetotelluric impedance tensors in the presence of local three-dimensional galvanic distortion. *J. Geophys. Res. Solid Earth* **1989**, *94*, 1913–1925. [[CrossRef](#)]
27. Groom, R.W.; Bailey, R.C. Analytic investigations of the effects of near-surface three-dimensional galvanic scatterers on MT tensor decompositions. *Geophysics* **1991**, *56*, 496–518. [[CrossRef](#)]
28. McNeice, G.; Jones, A. Multisite, multifrequency tensor decomposition of magnetotelluric data. *Geophysics* **2001**, *66*, 158–173. [[CrossRef](#)]
29. Rodi, W.; Mackie, R.L. Nonlinear conjugate gradients algorithm for 2-D magnetotelluric inversion. *Geophysics* **2001**, *66*, 174–187. [[CrossRef](#)]
30. Ledo, J. 2-D Versus 3-D Magnetotelluric Data Interpretation. *Surv. Geophys.* **2005**, *26*, 511–543. [[CrossRef](#)]
31. Egbert, G.D.; Kelbert, A. Computational recipes for electromagnetic inverse problems. *Geophys. J. Int.* **2012**, *189*, 251–267. [[CrossRef](#)]
32. Kelbert, A.; Meqbel, N.; Egbert, G.D.; Tandon, K. ModEM: A modular system for inversion of electromagnetic geophysical data. *Comput. Geosci.* **2014**, *66*, 40–53. [[CrossRef](#)]
33. Yang, Y.; Li, Y.; Liu, T.; Zhan, Y.; Feng, J. Interactive 3D forward modeling of total field surface and three-component borehole magnetic data for the Daye iron-ore deposit (Central China). *J. Appl. Geophys.* **2011**, *75*, 254–263. [[CrossRef](#)]
34. Wang, P.; Algeo, T.J.; Zhou, Q.; Yu, W.; Du, Y.; Qin, Y.; Xu, Y.; Yuan, L.; Pan, W. Large accumulations of 34S-enriched pyrite in a low-sulfate marine basin: The Sturtian Nanhua Basin, South China. *Precambrian Res.* **2019**, *335*, 105504. [[CrossRef](#)]
35. Zhou, X.J.; Li, S.Z.; Wang, Y.J.; Liu, J. Tectonic Features of the Fanjing Mount and Sangzhi Area on the West of Xuefeng Uplift. *Earth Sci.* **2011**, *20*, 985–992. (In Chinese with English Abstract)
36. Cavagna, S.; Clari, P.; Martire, L. The role of bacteria in the formation of cold seep carbonates: Geological evidence from Monferrato (Tertiary, NW Italy). *Sediment. Geol.* **1999**, *126*, 253–270. [[CrossRef](#)]
37. Campbell, K.; Farmer, J.; Des Marais, D. Ancient hydrocarbon seeps from the Mesozoic convergent margin of California: Carbonate geochemistry, fluids and paleoenvironments. *Geofluids* **2002**, *2*, 63–94. [[CrossRef](#)]
38. Yu, W.; Algeo, T.J.; Du, Y.; Maynard, B.; Guo, H.; Zhou, Q.; Peng, T.; Wang, P.; Yuan, L. Genesis of Cryogenian Datangpo manganese deposit: Hydrothermal influence and episodic post-glacial ventilation of Nanhua Basin, South China. *Palaeogeogr. Palaeoclimatol. Palaeoecol.* **2016**, *459*, 321–337. [[CrossRef](#)]
39. Ma, Z.; Liu, X.; Yu, W.; Du, Y.; Du, Q. Redox conditions and manganese metallogenesis in the Cryogenian Nanhua Basin: Insight from the basal Datangpo Formation of South China. *Palaeogeogr. Palaeoclimatol. Palaeoecol.* **2019**, *529*, 39–52. [[CrossRef](#)]

40. Corsetti, F.; Lorentz, N. On Neoproterozoic Cap Carbonates as Chronostratigraphic Markers. In *Neoproterozoic Geobiology and Paleobiology*; Springer: Dordrecht, The Netherlands, 2006; pp. 273–294.
41. Chen, X.; Li, D.; Ling, H.-F.; Jiang, S.-Y. Carbon and sulfur isotopic compositions of basal Datangpo Formation, northeastern Guizhou, South China: Implications for depositional environment. *Prog. Nat. Sci.* **2008**, *18*, 421–429. [[CrossRef](#)]
42. Yu, W.; Algeo, T.J.; Du, Y.; Zhou, Q.; Wang, P.; Xu, Y.; Yuan, L.; Pan, W. Newly discovered Sturtian cap carbonate in the Nanhua Basin, South China. *Precambrian Res.* **2017**, *293*, 112–130. [[CrossRef](#)]
43. Kennedy, M.; Christie-Blick, N.; Sohl, L. Are Proterozoic Cap Carbonates and Isotopic Excursions a Record of Gas Hydrate Destabilization Following Earth's Coldest Intervals. *Geology* **2001**, *29*, 443–446. [[CrossRef](#)]
44. Jiang, G.; Kennedy, M.; Christie-Blick, N. Stable isotopic evidence for methane seeps in Neoproterozoic postglacial cap carbonates. *Nature* **2003**, *426*, 822–826. [[CrossRef](#)]
45. Jiang, G.; Sohl, L.; Christie-Blick, N. Neoproterozoic stratigraphic comparison of the Lesser Himalaya (India) and Yangtze block (South China): Paleogeographic implications. *Geology* **2003**, *31*, 917–920. [[CrossRef](#)]
46. Kennedy, M.; Mrofka, D.; Borch, C. Snowball Earth termination by destabilization of equatorial permafrost methane clathrate. *Nature* **2008**, *453*, 642–645. [[CrossRef](#)] [[PubMed](#)]